Dynamics in Psoralen-Damaged DNA by ^{1}H-Detected Natural Abundance ^{13}C NMR Spectroscopy†

H. Peter Spielmann*

Departments of Biochemistry and Chemistry, University of Kentucky, Lexington, Kentucky 40536-0084

Received October 14, 1997; Revised Manuscript Received January 16, 1998

ABSTRACT: The dynamics of the DNA oligomer d(GCGTACGC)$_2$ and the 4′-(hydroxymethyl)-4,5′,8-trimethylpsoralen−DNA furanside monoadduct (MAf) of this oligomer have been determined from NMR relaxation parameters. Longitudinal and transverse ^{13}C relaxation rates and heteronuclear NOE relaxation data have been measured at natural abundance and have been analyzed in the context of the Lipari and Szabo model-free formalism. The generalized order parameters for methine carbons in the octamer sequence d(GCGTACGC)$_2$ (UM) are relatively and uniformly high for the entire molecule. The generalized order parameters for methine carbons in the MAf are significantly lower for the deoxyribose bearing the damaged thymidine base and for the bases flanking the lesion on the undamaged strand, indicating additional conformational flexibility due to the lesion. The order parameters for the bases on the damaged strand flanking the lesion remain high. Analysis of the relaxation data indicates substantial chemical exchange for the adenosine residues in the UM TpA site, and this chemical exchange is quenched upon MAf formation. These data are discussed in terms of a model for DNA damage recognition by the nucleotide excision repair system.

A complete understanding of the effects of DNA damage must include a quantitative description of both normal nucleic acid dynamics and alterations that occur at lesion sites. Several studies have shown that DNA exhibits sequence dependent structural and conformational polymorphism in solution. These conformational equilibria may play a significant role in the interaction of DNA with specific proteins and small molecule ligands. NMR[1] relaxation experiments can provide a wealth of information on both the structure and conformational equilibria of DNA in solution, and several studies have attempted to describe the internal motions of the DNA backbone (*1*−*4*), of sugar repuckering (*4*, *5*), and of base-pair opening (*6*−*8*). Precise conclusions were difficult to deduce from these studies because there are usually several motions taking place simultaneously with different amplitudes and on different time scales extending from picosecond to second. Additionally, the correlations between atomic motion and nucleic acid function are not completely understood.

Although a number of experimental techniques can characterize internal motions in nucleic acids, NMR is uniquely useful because a large number on nuclear sites within a given molecule can be simultaneously studied over a wide range of time scales (*9*). For example, information about fast internal motions and overall rotational tumbling of a molecule in solution can be obtained from ^{13}C NMR relaxation measurements. These measurements, however, are difficult to achieve directly because of crowding in the spectra of biological macromolecules and the low natural abundance (1.1%) and decreased sensitivity of ^{13}C nuclei (one-fourth that of protons). The introduction of two-dimensional proton-detected heteronuclear techniques has reduced some of the problems due to the inherent lack of sensitivity of ^{13}C nuclei and the limited resolution of one-dimensional NMR techniques [reviewed by Bax et al. (*10*)]. Recently, investigations of NMR relaxation have been carried out for ^{13}C nuclei at natural abundance in various proteins (*11*−*14*, *60*) and by direct carbon detection for some DNA oligomers (*5*). Selective ^{13}C labels have been incorporated into DNA oligomers at the C1′ position, and their relaxation and dynamic behavior has been measured (*15*).

Damaged DNA is of particular interest because of the severe distortions introduced by the lesion into the structure of the molecule. Major questions are how this damage affects the structure of the polymer and how DNA changes conformation to absorb the impact of the damage. Damaged nucleic acids are recognized by and are tightly bound by the recognition element of the nucleotide excision repair system (NER), and this process is expected to depend on structural and dynamic properties of the damaged DNA as well as those of the protein components of the excinuclease.

The nucleotide excision repair system is responsible for the removal of most DNA lesions in all cellular organisms and is active in all cellular organisms (*16*, *17*). NER relies

† This work was supported in part by American Cancer Society Grant IN-163 and the Kentucky-NSF EPSCoR Program (EPS-9452895).

* E-mail: hps@pop.uky.edu. Phone: (606) 257-4790. Fax: (606) 323-1037.

[1] Abbreviations: dsDNA, double-stranded DNA; EDTA, ethylenediaminetetraacetic acid; NMR, nuclear magnetic resonance; NOE, nuclear Overhauser effect; NOESY, nuclear Overhauser effect spectroscopy; HMT, 4′-(hydroxymethyl)-4,5′,8-trimethylpsoralen; TMP, 4,5′,8-trimethylpsoralen; COSY, correlation spectroscopy; UM, unmodified DNA oligomer 5′-GCGTACGC-3′; MAf, psoralen furanside monoadduct; XL, psoralen interstrand cross-link; DQF−COSY, double-quantum-filtered correlation spectroscopy; NER, nucleotide excision repair; DEPT, distortionless enhancement by polarization transfer; HMQC, heteronuclear multiple-quantum coherence.

S0006-2960(97)02536-1 CCC: $15.00 © 1998 American Chemical Society
Published on Web 04/01/1998

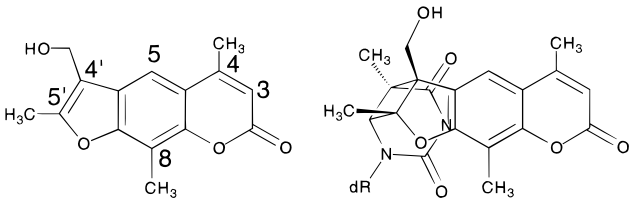

FIGURE 1: 4′-(hydroxymethyl)-4,5′,8-trimethylpsoralen (HMT) (**1**) and the HMT−thymidine furanside monoadduct (MAf) (**2**).

on the redundant information in the DNA duplex to remove a damaged nucleotide and replace it with a normal nucleotide by using the complementary strand as a template. The NER system functions by (1) recognizing that the DNA is damaged, (2) specifically binding to the lesion, and (3) hydrolyzing two phosphodiester bonds on either side of the lesion to generate an oligonucleotide containing the damage. The excised oligonucleotide is released from the duplex, and the resulting gap is subsequently filled in and ligated to complete the repair. The NER systems in humans (*XP* complementation group), yeast (*RAD* complex), and *Escherichia coli* [*uvr (A)BC*] share a remarkably similar mechanism and repertoire of substrates; however, there is no sequence or subunit homology between the eukaryotic and prokaryotic systems (*16*). NER efficiently recognizes and removes many structurally diverse DNA damaging agents, while the wide range of normal DNA microstructures triggers a response that is *3*−*5* orders of magnitude lower in rate (*18*−*21*).

Psoralens are a class of photomutagenic (*22*−*26*) and photochemotherapeutic (*27*−*30*) molecules that covalently modify nucleic acids. They belong the family of small molecules that intercalate into and photoalkylate double-stranded DNA. The primary targets of psoralens are thymidine residues, and these molecules form both monoadducts and interstrand cross-links. The reaction takes place between the 3,4 (pyrone) or 4′,5′ (furan) double bonds of the psoralen and the 5,6 double bond in pyrimidines (*31*−*34*). The effects of psoralen adducts on the structure and function of DNA have been extensively studied (*35*−*42*). Psoralen-damaged DNA is recognized by both the human repair system and the prokaryotic (A)BC excinuclease and serves as an excellent model to study the structural and dynamic motifs that cellular repair enzyme systems may recognize (*17*, *40*−*44*). Previous studies have shed light on the mechanism of psoralen adduct formation and their biological consequences (*17*, *45*−*50*).

4′-(Hydroxymethyl)-4,5′,8-trimethylpsoralen (HMT, **1**) (Figure 1) is a synthetic psoralen derived from the natural product 4,5′,8-trimethylpsoralen (TMP). HMT has greatly enhanced water solubility relative to TMP and forms high yields of adducts with DNA. The structures of both the HMT furanside monoadducted (MAf) and interstrand cross-linked (XL) dsDNA molecules have been determined by NMR spectroscopy and restrained molecular dynamics (*40*, *41*). Comparisons of the structural and dynamic differences between the UM and the MAf allow for examination of features that may be recognized by the enzyme system. Understanding how the NER excinuclease recognizes psoralen damage to DNA will assist in the elucidation of the general mechanism of lesion recognition. The photobinding of HMT to dsDNA results in substantial structural distortion to the normal B-form DNA helix. This distortion is hypothesized to be responsible for changes in the DNA structure that allow for the recognition of the damage by the nucleotide excision repair system. Direct recognition of the HMT lesion by the repair proteins is unlikely because a wide variety of DNA lesions that do not share common structural features are recognized and removed from DNA by NER (*18*, *51*). A proposed mechanism for the recognition of damage by NER involves the recognition of altered backbone conformations that are only accessible to damaged DNA and not normal DNA (*19*, *20*, *51*−*53*).

The three-dimensional structures of the MAf and the photoisomeric XL show that the conformational differences between undamaged DNA and the adducted molecules are localized to within three base pairs of the damage. Results from previous ^{1}H NMR experiments on these systems suggest that damage results in conformational heterogeneity for the nearby sugar residues (*40*, *41*, *54*). These results suggest that characterization of the changes in nucleic acid dynamics may be important for understanding DNA damage and repair.

This paper reports on a study of the dynamics of the undamaged oligomer (UM) and the HMT monoadducted (MAf) DNA oligomer d(GCGTACGC)$_2$ based on ^{13}C relaxation measurements made by using proton-detected ^{13}C−^{1}H 2D NMR spectroscopy. The data for the UM and the MAf are compared with each other and with other relaxation data available for other DNA molecules. This study forms the background for a comparative analysis with other types of DNA damage that is recognized by the NER system. These comparisons will provide detailed information on the changes in structure and dynamics that occur as a result of damage to the DNA helix and will suggest mechanisms used for recognition of this damage by repair systems.

EXPERIMENTAL PROCEDURES

Materials. The MAf was prepared as described in Spielmann et al. (*55*). The following numbering scheme describes the residues in the UM, MAf, and XL:

```
5'- G1  C2  G3  T4  A5  C6  G7  C8 -3'

3'- C16 G15 C14 A13 T12 G11 C10 G9 -5'
```

T4 is modified in the MA, and in the XL both T4 and T12 are covalently connected through the psoralen. All measurements on the UM and MAf were made on one 4 mM sample and on one 3 mM sample, respectively, in 99.9% D_2O adjusted to pH 7.0, 20 mM PO_4^-, 10 mM NaN_3, 100 mM NaCl, and 0.1 mM EDTA.

Structural Coordinates. The atomic coordinates for the MAf were obtained from PDB entry 203D (*41*). Models for the UM were generated using standard Arnott parameters for B-form DNA in the Biopolymer module of insightII (version 2.3.0) (Biosym Technologies, San Diego).

Acquisition of NMR Spectra. Experiments were recorded at 298 K on a Varian Inova 500 (11.74 T) spectrometer. The ^{13}C spin−lattice (R_1) and spin−spin (R_2) relaxation rate constants and steady-state {^{1}H}−^{13}C NOEs were measured from ^{1}H-detected ^{1}H−^{13}C correlation spectra with DEPT-

type transfer of magnetization and allow for the suppression of unwanted ^{1}H resonances bonded to ^{12}C prior to detection and for elimination of the residual solvent signal (*12*, *14*).

Representative proton T_1 values were determined by the inversion recovery method from 1D spectra (data not shown). High digital resolution HMQC spectra of the UM were acquired without ^{13}C decoupling to measure the ^1J ^{13}C−^{1}H coupling constants (data not shown).

All relaxation spectra were recorded with a spectral width of 4489.3 Hz and 1024 real points in ω_2; digital oversampling by a factor of 40 was employed to reduce baseline distortions associated with the spectrometer's low-pass filters (*56*). All experiments were recorded using the hypercomplex method of phase incrementation to obtain quadrature phase detection in ω_1 (*57*). A spectral width of 2700 Hz was used in ω_1 that led to extensive folding of the spectrum (*58*), and 64 complex points were collected. For all experiments the value of Δ for the DEPT polarization transfers was set to 2.78 ms, corresponding to a maximum magnetization transfer for $^1J = 180$ Hz that was the average of the anomeric and the aromatic carbon−proton one bond coupling constants. Decoupling of ^{13}C during acquisition was performed using the GARP-1 scheme built into the spectrometer hardware. For the R_1 and R_2 measurements the relaxation delays in the pulse sequences were set to 3.4 s (approximately 1.9 times the average ^{1}H spin−lattice relaxation time of 1.78 s, except for the adenine H2 protons which had a ^{1}H T_1 of 5.0 s), and the total number of transients recorded per t_1 point was 256 and 512 for real and complex data, respectively. For the {^{1}H}−^{13}C NOE measurements the ^{1}H recovery period prior to acquisition was 4.0 s (greater than 8 times the longest ^{13}C spin−lattice relaxation time), and the total number of transients recorded per t_1 point was 1024 and 2048 for real and complex data, respectively.

Two spectra, one with and one without ^{1}H saturation, were recorded in an interleaved manner to yield heteronuclear steady-state {^{1}H}−^{13}C NOEs which were acquired over a 12-day period. To measure R_1, nine experiments with relaxation delays T of 0.01, 0.038, 0.073, 0.143, 0.213, 0.423, 0.633, 0.948, and 1.893 s were recorded in an interleaved manner over a 13-day period. Monoexponential evolution of carbon magnetization was obtained by saturation of the protons by applying π pulses every 7 ms during the recovery delay in the T_1 experiments (*14*). T_2 experiments were performed with a Carr−Purcell−Meiboom−Gill (CPMG) spin−echo sequence with nine transverse relaxation delays T of 1, 5, 10, 15, 20, 30, 40, 50, and 60 ms in an interleaved manner over a 13-day period. A second T_2 experiment for the MAf was performed with nine transverse relaxation delays T of 1, 5, 7.5, 10, 12.5, 15, 20, 25, and 30 ms in an interleaved manner over a 13-day period. The CPMG sequence was not modified to suppress the effects of cross-correlation between dipolar and chemical shift anisotropy (CSA) relaxation mechanisms (*59*).

Data Processing. Felix (Biosym, San Diego) was used for data processing. A cosine bell function was applied to the first 512 complex data points in each ω_2 FID. Prior to Fourier transformation the data were zero-filled once. In ω_1, the interferogram was extended to 128 complex points by linear prediction, followed by multiplication with a skewed sine bell phase shifted 60° and with a skew of 0.7.

Analysis of Relaxation Rate Constants and NOEs. Intensities of the resonance peaks in the two-dimensional spectra were determined as peak heights. The uncertainties in the measured peak heights (σ_h) were taken to be the rmsd baseplane noise in the spectra. These values are generally underestimated in comparison with those obtained from duplicate data points. However, the limitations imposed by ^{13}C at natural abundance precluded the acquisition of replicate measurements.

The relaxation rate constants were obtained from nonlinear fits of monoexponential equations for longitudinal and transverse relaxation (eqs 1−3) using the Levenburg−Marquardt algorithm as described (*12*). The measured peak intensities for different delays from the R_1 experiments were fit to

$$I(T) = I_\infty - (I_\infty - I_0)\mathrm{e}^{-R_1T} \tag{1}$$

and for R_2 to

$$I(T) = I_0\mathrm{e}^{-R_2T} \tag{2}$$

or to

$$I(T) = c + I_0\mathrm{e}^{-R_2T} \tag{3}$$

in which $I(T)$ is the intensity at time T, I_∞ is the intensity at time = infinity, and I_0 is the intensity at time = 0. The uncertainties in the values of R_1 and R_2 were determined as the formal standard deviations calculated from the covariance matrix in the nonlinear optimization routine. Steady-state NOEs were calculated as the ratios of the peak heights in the spectra recorded with and without proton saturation.

The monoexponential decay functions given by eqs 1−3 were evaluated with a χ^2 goodness-of-fit test, by comparing χ^2 to the 90% critical value of the χ^2 distribution as described by Palmer et al. (*12*). For the T_2 data, the significance of the improvement afforded by the three-parameter model (eq 3) over the two-parameter model (eq 2) was evaluated using an F statistic (*61*) defined as

$$F = (n - 3)(\chi_2{}^2 - \chi_3{}^2)/\chi_3{}^2 \tag{4}$$

where $\chi_m{}^2$ is the chi-squared goodness-of-fit statistic for the m-parameter model. None of the fits in these systems were statistically improved by the three-parameter fit as judged by the criteria that the F statistic was greater than the 95% critical value of the distribution of F values. The critical value was determined from 500 Monte Carlo simulations (*12*) and was approximately equal to 4.96 [the tabulated value of $F_{10,1,0.05}$ (*62*)].

Calculation of Model-Free Parameters. The relaxation of a methine ^{13}C nucleus at natural abundance at high field strengths is dominated by the dipolar interaction with the directly attached proton and by the CSA mechanism (*63*). The ^{13}C chemical shift tensor is approximately axially symmetric with the principal axis that is nearly collinear with the C−H bond. Consequently, the relaxation parameters are functions of the spectral density function $J(\omega)$, given by the Fourier transform of the orientational correlation function for a unit vector along the C−H bond, at the five characteristic frequencies of a two-spin system (*64*). The apparent spin−lattice relaxation rate constant, ignoring cross-correla-

tion effects, is the sum of the dipolar and the CSA spin−lattice rate constants. The apparent spin−spin relaxation rate constant, ignoring cross-correlation effects, is the sum of the dipolar and the CSA spin−spin relaxation rate constants plus the rate constant (R_{ex}) for other pseudo-first-order processes that contribute to the decay of transverse magnetization during the CPMG sequence (e.g., chemical exchange). The ^{13}C R_1 and R_2 relaxation rate constants and the NOEs are given by

$$R_1 = (d^2/4)[J(\omega_H - \omega_C) + 3J(\omega_C) + 6J(\omega_H + \omega_C)] + c^2J(\omega_C) \quad (5)$$

$$R_2 = (d^2/8)[4J(0) + J(\omega_H - \omega_C) + 3J(\omega_C) + 6J(\omega_H) + 6J(\omega_H + \omega_C)] + (c^2/6)[3J(\omega_C) + 4J(0)] + R_{ex} \quad (6)$$

$$\mathrm{NOE} = 1 + (d^2/4R_1)(\gamma_H/\gamma_C)[6J(\omega_H + \omega_C) - J(\omega_H - \omega_C)] \quad (7)$$

in which

$$d = (\mu_0 h/8\pi^2)\gamma_H\gamma_C(1/r_{CH}^3) \quad (8)$$

$$c = \omega_C(\sigma_{||} - \sigma_\perp)/\sqrt{3} \quad (9)$$

and μ_0 is the permeability of free space, h is Plank's constant, γ_H and γ_C are the gyromagnetic ratios of ^1H and ^{13}C, respectively, r_{CH} is the carbon−proton bond length (1.09 Å), ω_H and ω_C are the Larmor frequencies of ^1H and ^{13}C, and $\sigma_{||}$ and $\sigma_\perp$ are parallel and perpendicular components of the chemical shift tensor. The value of the chemical shift anisotropy ($\sigma_{||} - \sigma_\perp$) for ^{13}C depends on the type and hybridization of the atom. The estimated CSA for a sp^3-hybridized C1′ carbon is 41 ppm, while the estimated CSA for an sp^2 aromatic carbon is closer to 185 ppm (*15*, *65*). The T4C6 carbon is somewhat more problematic; although it formally has an sp^3 hybridization, the ring strain and geometry imposed by the cyclobutane ring probably place the value of the CSA tensor at greater than 41 ppm, but not nearly as large as the estimated aromatic CSA of 185 ppm. In this study, we set the MAf T4C6 carbon CSA to 41 ppm. These values are in contrast to the value of 25 ppm commonly used for the CSA of the Cα carbon in protein dynamics calculations. Contributions by CSA to relaxation for a CSA of between 10 and 50 ppm are negligible at 11.74 T, accounting for less than 5% of the relaxation rate (*15*). However, for a CSA of 185 ppm, such as the aromatic carbons, the contribution to relaxation can be more than 25% (*5*).

The amplitudes and time scales of intramolecular motions of individual C−H bond vectors for the UM and MAf were obtained by fitting the observed relaxation data to the extended Lipari and Szabo model-free formalism of the spectral density function (*12*). In this approach the dimensionless generalized order parameter S^2 is used to describe the spatial extent of motion of the C−H bond vector. S^2 ranges from 0 for completely free internal motion to 1 for completely restricted motion relative to the overall tumbling of the molecule in solution. The spectral density function cannot be determined explicitly using only the measured parameters R_1, R_2, and NOE. Instead, the relaxation data for each spin was analyzed by the model-free approach pioneered by Lipari and Szabo (*66*, *67*). Parsimonious relaxation models for each nuclear spin were chosen using the selection strategy outlined in Mandel et al. (*61*). Briefly, the three relaxation data for each spin (R_1, R_2, and NOE) are fit to each of five models having either two, one or no degrees of freedom that describe a subset of the extended Lipari and Szabo model-free eq 10 (*66*−*68*):

$$J(\omega) = \frac{2}{5}\left[\frac{S^2\tau_m}{1 + (\omega\tau_m)^2} + \frac{(1 - S^2_f)\tau'_f}{1 + (\omega\tau'_f)^2} + \frac{(S^2_s - S^2)\tau'_s}{1 + (\omega\tau'_s)^2}\right] \quad (10)$$

where $\tau'_f = \tau_f\tau_m/(\tau_f + \tau_m)$, $\tau'_s = \tau_s\tau_m/(\tau_s + \tau_m)$, τ_m is the overall rotational correlation time of the molecule, τ_f is the effective correlation time for internal motions on a fast time scale (τ_f <100−300 ps), τ_s is the effective correlation time for internal motions on a slow time scale ($\tau_f < \tau_s < \tau_m$), $S^2 = S^2_fS^2_s$ is the square of the generalized order parameter characterizing the amplitude of the internal motions, and S^2_f and S^2_s are the squares of the order parameters for the internal motions on the fast and slow time scales, respectively. Motions represented by S^2 refer to internal dynamics on the picosecond to nanosecond time scale. The effective correlation (either τ_f or τ_s) depends on the rate of motion of the C−H bond vector. A physical interpretation of τ_f or τ_s is generally difficult and requires reference to a specific motional model. R_{ex} has been included in eq 6 to account for the effects of chemical exchange and other pseudo-first-order processes such as conformational averaging on a time scale much slower than the overall rotational correlation time (τ_m) that contribute to the decay of transverse magnetization (*69*). The conformational exchange processes represented by R_{ex} will be referred to as dynamics on the microsecond to millisecond time scale in this analysis. Fitting experimental data using eq 10 requires a maximum of six free parameters, the five parameters in the equation and the chemical exchange term R_{ex} in eq 6. Mandel et al. describe five simpler dynamic models derived from eq 10 that contains an overall correlation time, a maximum of three internal motional parameters and a single internal time scale parameter, either τ_f or τ_s. The five models consist of the following subsets of the extended model free parameters in eq 10: (1) S^2; (2) S^2, τ_f; (3) S^2, R_{ex}; (4) S^2, τ_f, R_{ex}; (5) S^2, S^2_f, τ_s. Model 1 is appropriate if motions on the slow time scale are negligible and motions on the fast time scale are very fast (<20 ps). Model 2 is the original formulation of Lipari and Szabo (*66*) and is applicable if motions on the slow time scale are negligible. Models 3 and 4 are derived from models 1 and 2, respectively, by including a nonzero chemical exchange contribution, R_{ex}, in the relaxation model. For models 1−4 $S^2 = S^2_f$. Model 5 assumes only that $\tau_f \rightarrow 0$. We fit the three relaxation data for each spin (R_1, R_2, and NOE) to each of the five models using the program Modelfree (version 3.1) (*12*). With these data, there were two degrees of freedom for model 1, one degree of freedom for models 2 and 3, and no degrees of freedom for models 4 and 5. Selection of the most appropriate model to describe the data for each spin is described in detail in Mandel et al. (*61*) and basically consists of statistically evaluating the fit of the experimental data to each model and choosing the simplest model that best fits the data. This is a conservative

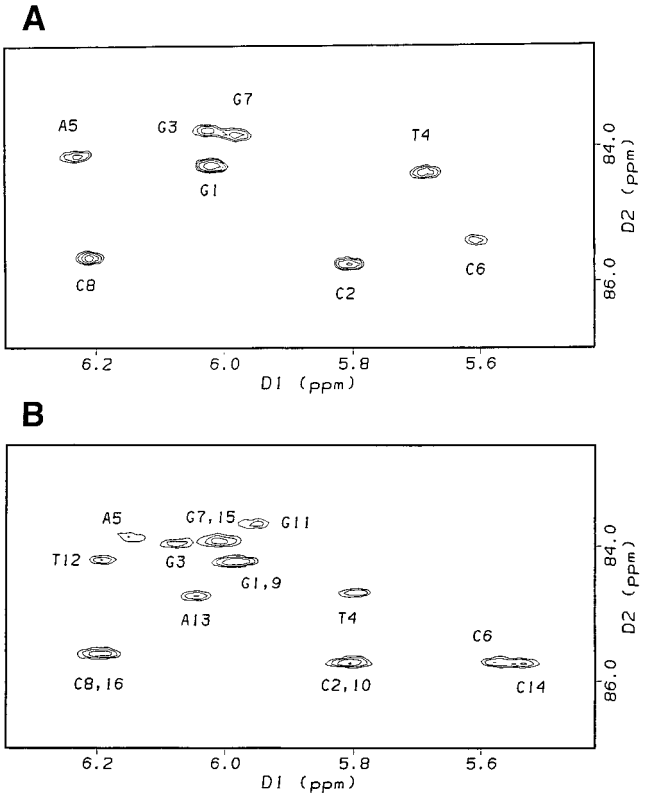

FIGURE 2: Deoxyribose C1′ portion of the $^{13}C-^{1}H$ correlation spectrum for (A) the UM and (B) the MAf from the pulse sequence used to measure R_1 with a delay of 1 ms.

model selection strategy which neither under- or overparametrizes the available data.

The model-free parameters were extracted by substitution of eq 10 into eqs 5−7 for R_1, R_2, and NOE, respectively, followed by nonlinear least-squares fitting of the experimental data. In this analysis, τ_m is assumed to be the same for all C−H bond vectors (isotropic tumbling), and the values for τ_s and τ_f are variable. The optimization minimized the function:

$$\chi^2 = \sum[(R_{1i} - R^c_{1i})^2/\sigma^2_{1i} + (R_{2i} - R^c_{2i})^2/\sigma^2_{2i} + (\eta_i - \eta^c_{1i})^2/\sigma^2_{\eta i}] \quad (11)$$

where the index, i, indicates the spin number, σ_{1i}, σ_{2i}, and $\sigma_{\eta i}$ are the uncertainties for the experimental relaxation parameters R_1, R_2, and NOE for spin number i, respectively, and R^c_{1i}, R^c_{2i}, and η^c_{1i} are the calculated relaxation parameters of residue i, respectively. Statistical properties of the model free parameters were obtained from Monte Carlo simulations using 500 randomly distributed synthetic data sets for R^c_{1i}, R^c_{2i}, and η^c_{1i}.

RESULTS

Carbon chemical shift assignments for the UM and MAf were obtained by correlating the ^{1}H chemical shift values obtained from analysis of NOESY and DQF-COSY spectra (*40*, *41*) with the ^{13}C chemical shifts from HMQC spectra. Spectra of the deoxyribose C1′ resonances for the MAf and UM are shown in Figure 2. The relaxation parameters, R_1, R_2, and NOE were obtained by analysis of proton-detected natural abundance $^{13}C-^{1}H$ heteronuclear correlation spectra

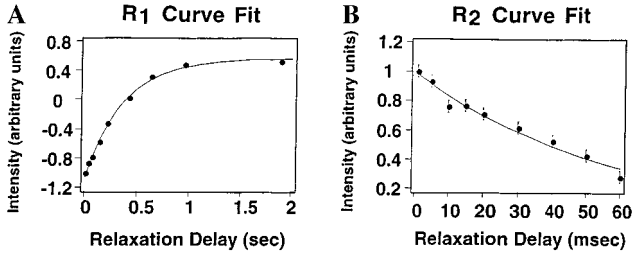

FIGURE 3: ^{13}C relaxation data for the HMT-C3: (A) R_1 relaxation decay curve, $R_1 = 2.73 \pm 0.0376\ s^{-1}$; (B) R_2 relaxation decay curve, $R_2 = 18.0 \pm 1.39\ s^{-1}$.

of the MAf and UM. The signal-to-noise ratio was calculated as the mean peak height in the 1 ms relaxation delay R_1 experiment, the 1 ms relaxation delay R_2 experiment, and the NOE experiment without proton saturation over the rms baseline noise in each spectrum, respectively. Mean values for the signal-to-noise ratios in the spectra for the MAf were 25.5, 26.6, and 20.9 for R_1, R_2, and NOE measurements, respectively. For the UM, the signal-to-noise ratios in the spectra were 94.5, 87.1, and 53.5 for R_1, R_2, and NOE measurements, respectively. Reliable quantitation of peak intensities for the UM was possible for all methine carbons in the molecule (aromatic, C1′, C3′, and C4′) except for G1C4′ and G3C4′, which were completely overlapped. Many fewer carbons in the MAf could be accurately quantified because of severe spectral overlap. The d(GCG-TACGC)$_2$ duplex (UM) has only eight spectroscopically distinct residues due to its self-complementary nature. The 2-fold symmetry of the UM duplex is broken by HMT adduct formation in the MAf. In the MAf, the HMT is covalently attached to T4 through a cyclobutane ring formed between the 5,6 double bond of the thymidine and the 4′,5′ double bond of the psoralen. In the MAf, the corresponding resonances for the terminal pseudo-symmetry-related G1/C16 and C8/G9 base pairs were degenerate, and most of the corresponding pseudo-symmetry-related resonances for the C2/G15 and G7/C10 base pairs were also degenerate. Some of the MAf resonances in and immediately adjacent to the damage site were well resolved and could be accurately quantified. Sample R_1 and R_2 relaxation decay curves for the MAf are shown in Figure 3.

Global Tumbling. Relaxation data were analyzed assuming isotropic overall rotational motion of both the MAf and UM, which assumes a spherical shape for the DNA oligomers in solution. Final optimization with the selected dynamic model for each nuclear spin gave a global τ_m of 3.30 ns for the UM and a global τ_m of 3.60 ns for the MAf. Optimizations converged to the same result for initial estimates of τ_m from 2 to 5 ns. The 10% trimmed mean R_2/R_1 ratios for the UM and MAf interpreted using the simple Lipari and Szabo formalism gave overall correlation times of 3.44 and 3.72 ns, respectively. The global τ_m calculated from the ^{13}C relaxation data compares favorably with the values that gave the best fit for the ^{1}H NOESY relaxation data that was converted to interproton distances using the RANDMARDI procedure used to determine the solution structure of the MAf (*40*, *41*, *70*). In that procedure, a τ_m of 3.75 ns for the MAf ^{1}H NOE data gave the best fit. The rotational correlation time τ_m for the self-complementary 8-mer 5′-GGGTACCC-3′ cross-linked with a nitroxide spin-label psoralen was calculated by simple line-height analysis of the EPR spectrum

Table 1: Backbone Dynamic Parameters for UM

atom	model[a]	S^2	τ_f	R_{ex}	Γ_i
G1C8	1	0.781 ± 0.015			4.12
C2C6	1	0.902 ± 0.021			2.30
C2C5	1	0.817 ± 0.016			7.43
G3C8	1	0.837 ± 0.016			1.35
T4C6	3	0.865 ± 0.012		1.51 ± 0.61	3.70
A5C8	3	0.782 ± 0.020		7.28 ± 1.52	2.87
A5C2	3	0.811 ± 0.015		2.73 ± 1.82	0.00
C6C6	1	0.896 ± 0.023			1.56
C6C5	1	0.741 ± 0.015			1.20
G7C8	2	0.746 ± 0.023	35 ± 13		0.06
C8C6	1	0.852 ± 0.018			3.01
C8C5	1	0.913 ± 0.023			0.85
G1C1′	2	0.689 ± 0.019	28 ± 5		0.43
C2C1′	2	0.796 ± 0.060	85 ± 54		1.56
G3C1′	3	0.912 ± 0.023		2.35 ± 1.28	5.99
T4C1′	2	0.775 ± 0.022	22 ± 9		0.45
A5C1′	2	1.000 ± 0.022	0 ± 64		4.20
C6C1′	2	0.770 ± 0.025	63 ± 13		0.58
G7C1′	2	0.886 ± 0.028	91 ± 34		0.17
C8C1′	4	0.696 ± 0.020	30 ± 6	2.78 ± 0.79	0.00
G1C3′	2	0.912 ± 0.023	82 ± 33		0.46
C2C3′	2	0.806 ± 0.024	54 ± 11		0.59
G3C3′	2	0.738 ± 0.019	34 ± 7		2.72
T4C3′	2	0.653 ± 0.014	42 ± 4		0.44
A5C3′	3	0.840 ± 0.017		10.2 ± 4.30	2.17
C6C3′	2	0.562 ± 0.016	26 ± 3		2.23
G7C3′	2	0.732 ± 0.019	35 ± 7		1.82
C8C3′	2	0.440 ± 0.020	25 ± 3		1.58
C2C4′	4	0.607 ± 0.014	30 ± 3	1.60 ± 0.53	0.00
T4C4′	4	0.753 ± 0.017	33 ± 5	4.69 ± 1.57	0.00
A5C4′	2	0.829 ± 0.023	40 ± 14		1.02
C6C4′	4	0.764 ± 0.022	63 ± 8	4.74 ± 1.90	0.00
G7C4′	2	0.766 ± 0.018	58 ± 9		0.00
C8C4′	2	0.675 ± 0.018	59 ± 6		0.27

[a] Dynamic models employed to fit the relaxation data for each nuclear spin as described in the text and Mandel et al. (*61*).

Table 2: Backbone Dynamic Parameters for MAf

atom	model[a]	S^2	τ_f	R_{ex}	Γ_i
C2C5	1	0.740 ± 0.049			3.09
G3C8	1	0.837 ± 0.056			0.66
T4C6	1	0.744 ± 0.132			1.80
A5C8	1	0.767 ± 0.082			0.12
A5C2	1	0.700 ± 0.065			1.51
C6C6	1	0.779 ± 0.069			5.26
C6C5	1	0.699 ± 0.052			2.59
C10C5	2	0.568 ± 0.054	87 ± 25		0.00
T12C6	4	0.659 ± 0.073	46 ± 27	4.69 ± 2.85	0.00
A13C8	1	0.703 ± 0.048			9.29
A13C2	1	0.797 ± 0.072			4.48
C14C6	1	0.841 ± 0.064			1.93
C14C5	1	0.769 ± 0.054			0.65
G3C1′	1	0.874 ± 0.065			0.35
T4C1′	4	0.645 ± 0.059	56 ± 21	5.02 ± 2.53	0.00
A5C1′	1	0.932 ± 0.021	18 ± 6		2.68
C6C1′	4	0.694 ± 0.062	54 ± 23	3.28 ± 1.62	0.00
G11C1′	1	0.940 ± 0.061			2.50
T12C1′	3	0.684 ± 0.070		3.59 ± 2.08	0.03
A13C1′	2	0.725 ± 0.047	60 ± 21		0.10
C14C1′	1	0.741 ± 0.043			3.45
HMTC3	1	0.704 ± 0.040			0.61
HMTC5	1	0.823 ± 0.056			0.88

[a] Dynamic models employed to fit the relaxation data for each nuclear spin as described in the text and Mandel et al. (*61*).

to be 2.5 ns (*42*). The rotational correlation times calculated from the ^{13}C relaxation data are also longer than those estimated by either fluorescence for oligomers of similar size or the Stokes−Einstein model values (*71*). The discrepancies in τ_m values probably arise from a number of causes, including simplifying assumptions introduced for each model, and we consider these estimates for the τ_m to be in acceptable agreement.

Dynamic Parameters. Optimized values of the model-free parameters are given in Table 1 for the UM and in Table 2 for the MAf. The lower precision of the parameters calculated for the MAf relative to the UM is a direct reflection of the lower signal-to-noise ratios in the spectra of the MAf. Order parameters are mapped onto the three-dimensional structures of the UM and MAf in panels A and B of Figure 4, respectively, using a pseudo-color representation. Chemical exchange terms are mapped onto the three-dimensional structures of the UM and MAf in panels A and B of Figure 5, respectively, using a pseudo-color representation.

The order parameters calculated indicate that the aromatic atoms in the UM are highly constrained on the fast motion time scale with an average $S^2 = 0.829 \pm 0.018$. The least constrained spin was the C6(14)C5 and the most highly constrained spin was the C8(16)C5 (Table 1). Only a subset of 13 of these spins in the MAf was resolved, and the average $S^2 = 0.739 \pm 0.020$, where the C10C5 spin was the least constrained and the C14C6 spin the most highly constrained (Table 2). The corresponding subset of spins in the UM had an average $S^2 = 0.820 \pm 0.014$. This is a significant decrease in the average order parameter for these residues in the MAf. All the resolved spins in the MAf except for the C10 and C2 C5 atoms are in the HMT-damaged center of the helix (see Table 2 and Figure 5).

The order parameters calculated indicate that the deoxyribose C1′ atoms in the UM are highly constrained on the fast motion time scale with an average $S^2 = 0.815 \pm 0.018$, similar to that of, but with a wider range than, the aromatic atoms, ranging from a low for G1(9)C1′ to a high for A5(13)C1′. Only a subset of eight of these spins in the MAf was resolved, and the average for these spins in the MAf was $S^2 = 0.779 \pm 0.039$. Both the T4C1′ and T12C1′ atoms had low order parameters while the A5C1′ atom had an order parameter similar to that in the UM. The corresponding subset of spins in the UM was even more constrained than those in the overall UM with an average $S^2 = 0.864 \pm 0.034$. This is a significant decrease in the average order parameter for these residues in the MAf where all the observed nuclei are in the HMT-damaged center of the helix.

Interestingly, the S^2 for the C1′, C3′, and C4′ spins in the various residues of the UM are not related in any simple way and are shown graphically in Figure 8. There are clearly sequence context dependent variations in the flexibility of the DNA polymer. This observation is consistent with the idea that microheterogeneity in the dynamics of DNA may correlate with structure. Except for the G1 residue, the C3′ and C4′ sugar carbons exhibit either greater or equal conformational freedom than that of the C1′ carbons. This may be because the non-C1′ carbons are not as highly constrained as the C1′ is by the attached base. Unfortunately, we cannot extend this analysis to the MAf because we cannot resolve the resonances for the C3′ and C4′ spins.

The order parameters for the aromatic and sugar spins in the central TpA base-pair step for the UM are very high. However, there are significant chemical exchange compo-

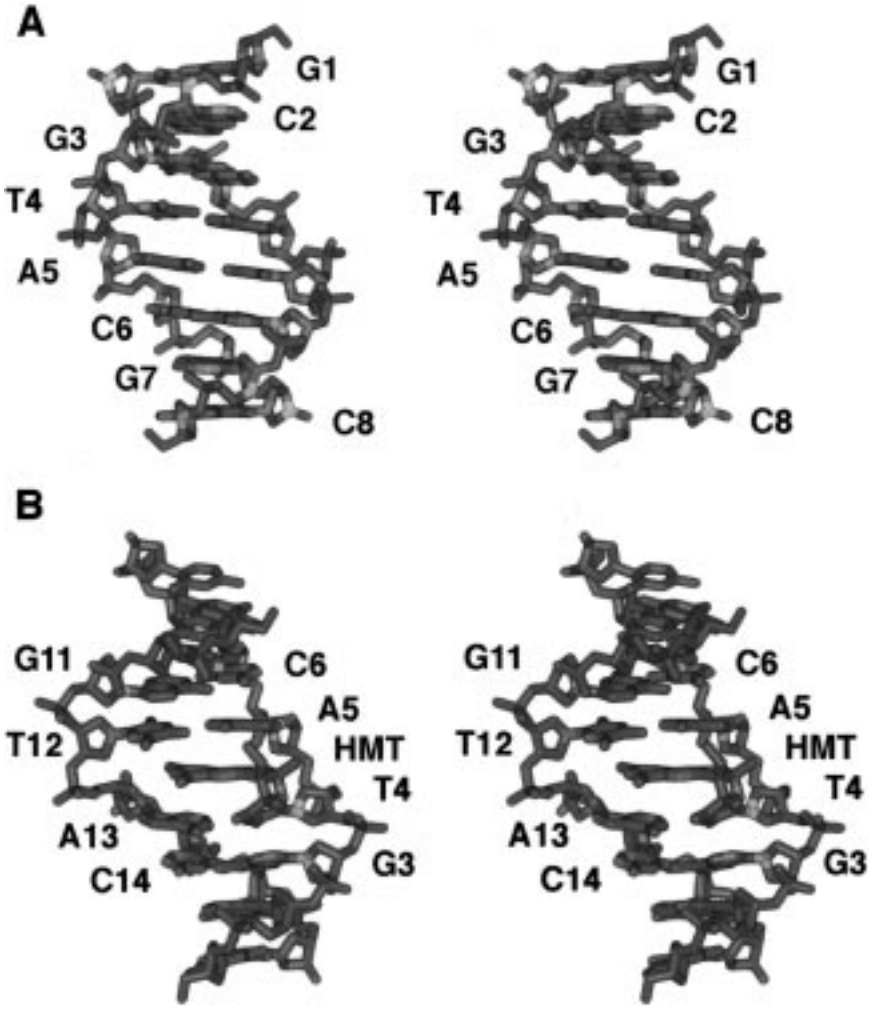

FIGURE 4: (A) Stereoview of the UM color-coded by the value of the generalized order parameter where the protons have been omitted for clarity. The structural coordinates were obtained from cannonical B-form coordinates. (B) Stereoview of the MAf color-coded by the value of the generalized order parameter where the protons have been omitted for clarity. The structural coordinates were obtained from PDB entry 203D (*41*). The color scheme is as follows: blue, S^2 not determined; cyan, $S^2 \geq 0.85$; green, $0.85 \geq S^2 \geq 0.75$; red, $0.75 \geq S^2 \geq 0.65$; yellow, $S^2 \leq 0.65$.

nents calculated for these spins (see below). TpA base-pair steps are the thermodynamically least stable of the base-pair steps (*72*) due in part to poor stacking interactions. This instability does not seem to manifest itself as disorder on the picosecond to nanosecond time scale, but rather as significant microsecond to millisecond time scale dynamics. There are particular indications of destabilization of the TpA step in the UM but not in the MAf (see discussion of chemical exchange below).

Chemical Exchange in the UM and MAf. There are a number of spins that require the inclusion of a significant R_{ex} term for an adequate fit to the experimental data to a dynamic model (Tables 1 and 2). The inclusion of an R_{ex} term in the model-free formalism generally accounts for such effects as chemical exchange and conformational averaging. However, the R_{ex} values reported here are not directly measured and are the results of correction terms to R_2 experimental data to achieve a better fit between theory and experiment. Even so, a relatively large R_{ex} value may indicate the existence of an intramolecular conformational exchange process. In numerous studies on the backbone dynamics in proteins, values of $R_{ex} > 1$ Hz are considered significant and are interpreted as indicating that these spins undergo significant dynamic processes in the microsecond to millisecond time regime. Using these criteria, we find that 9 of the 34 resolved spins in the UM have significant microsecond to millisecond dynamic processes (Figure 5A). Of the 23 spins that were analyzed for the MAf, 4 spins showed significant microsecond to millisecond dynamic processes (Figure 5B).

Fitting the relaxation data to the Lipari and Szabo formalism requires that the UM T4 and A5 aromatic C−H vectors have chemical exchange components. These are largest for the adenine, especially for the aromatic C8. It is clear from examination of the results for the UM that the central TpA step of the UM is destabilized relative to the other base-pair steps in the molecule (Figures 4B and 5B). Interestingly, this does not manifest itself in the calculated order parameters, but rather in the chemical exchange terms. These results are consistent with previous ^{1}H NMR studies which have shown that adenine bases at TpA steps experience large amplitude (20−50°) microsecond to millisecond time scale motions (*73*−*75*). The requirement for including a chemical exchange component to fit the UM relaxation data disappears upon HMT monoadduct formation, requiring only S^2 (Figures 4B and 5B). The implications are that the microsecond to millisecond dynamics present for the adenine bases in the UM TpA step are quenched by the formation

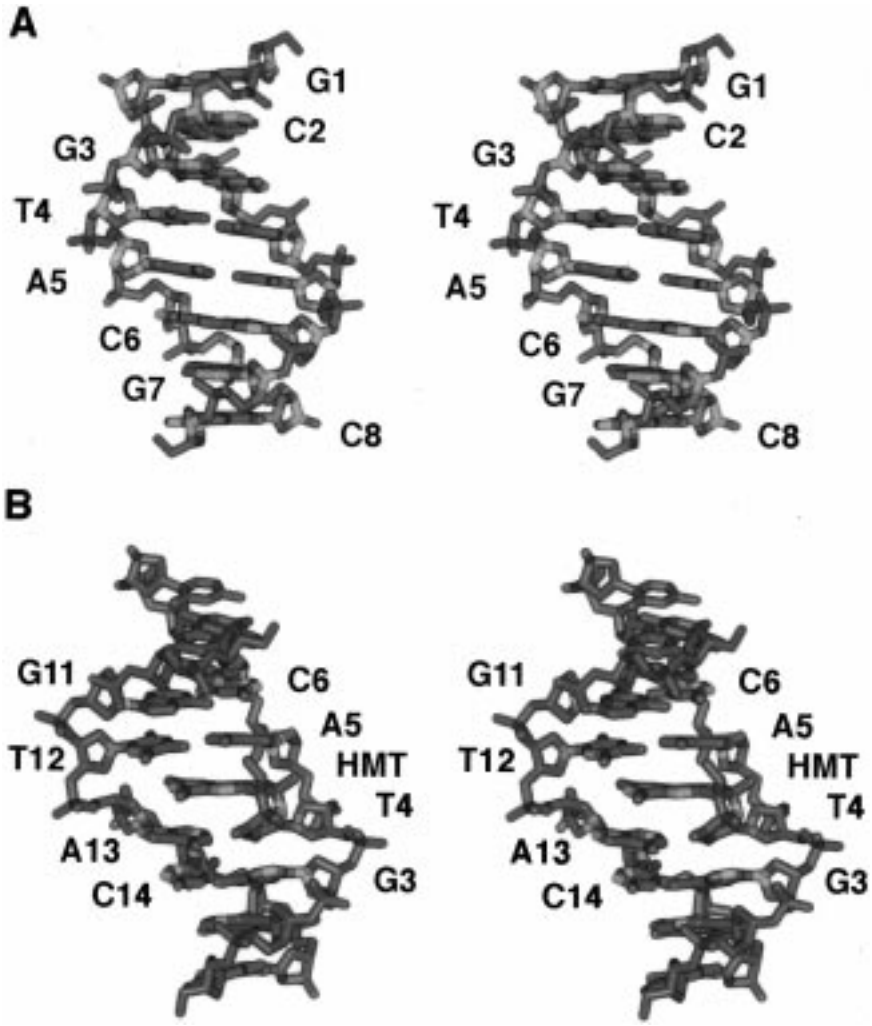

FIGURE 5: (A) Stereoview of the UM color-coded by the value of the chemical exchange term, R_{ex}, where the protons have been omitted for clarity. (B) Stereoview of the MAf color-coded by the value of the chemical exchange term, R_{ex}, where the protons have been omitted for clarity. The color scheme is as follows: blue, R_{ex} not determined; cyan, $R_{ex} = 0.0$ s^{-1}; green, $0.0 > R_{ex} > 2.0$; red, $2.0 > R_{ex} > 6.0$; yellow, $R_{ex} > 6.0$.

of the monoadduct. Structurally, this can be rationalized by the significant stacking interactions observed between the adenine bases and the HMT in the MAf structure (Figures 4B and 5B).

Fitting the relaxation data for the UM T4(12)C6 requires the inclusion of an R_{ex} term, while no R_{ex} term is required to fit the data for the MAf T4C6 and a substantially increased R_{ex} term is required for the MAf T12C6 (Tables 1 and 2). Fitting the relaxation data for the HMT-C3 and HMT-C5 spins to a dynamic model does not require the inclusion of an R_{ex} term. The T4C6 in the MAf is part of the MAf cyclobutane ring while the T12C6 is on the unmodified strand 3.35 Å away from the HMT pyrone ring. The 3.47 Å separation between the T12 C-5 and MAf C-4 and the 3.35 Å separation of T12 C-6 and MAf C-3 change to 1.54 Å each upon XL formation. T12 does not stack fully onto the HMT of the MAf and shows a substantial buckle in the NOE-derived structure (Figures 4B and 5B). While this buckle maximizes the van der Waals contacts with the HMT and G11 in the static average structure, it is possible that the base is undergoing a change in conformation that alternately has it fully stacked onto the G11 and then moved down to maximize contact with the HMT as shown in the structure. These data and the R_{ex} terms required to fit the data for the TpA step in the UM support the observation that poor stacking interactions may lead to significant dynamics in the microsecond to millisecond time regime. Due to the structural changes induced by monoadduct formation, the MAf C10-G11 base step becomes somewhat unstacked relative to the UM. This manifests itself in a significant decrease in the order parameter for C10C5 from 0.817 ± 0.016 in UM to 0.568 ± 0.054 in the MAf. However, there is no requirement for an R_{ex} term to fit the observed relaxation data. The results for the aromatic spins in the TpA site stand in contrast to the C1′ spins. There is no R_{ex} term required for the UM T4(12)C1′, which changes dramatically to 5.02 ± 2.53 s^{-1} for MAf T4C1′ and to 3.59 ± 2.08 s^{-1} for MAf T12C1′.

Motional Model for the Nucleotide Residues. The purine C8 and pyrimidine C6 atom order parameters for the UM are not correlated in any simple way with the C1′ order parameters, while in the MAf there is a reasonable correlation between S^2 for the C1′ and aromatic spins. However, there are three aromatic spins in the MAf for which the S^2 values are less well correlated with the attached C1′ carbon. The A5C8 and A5C2 spins in the MAf are much less ordered than the A5C1′, and the HMT-C5 is much more ordered than the T4C1′ (Table 2). Similar results for the UM A5(13)C8

Table 3: S^2 Parameters for MAf and UM

	MAf aromatic S^2	θ	UM aromatic S^2	θ	$\Delta\theta$
T12C6	0.659 ± 0.073	30 ± 4	0.865 ± 0.012	18 ± 1	12
HMT-C3	0.704 ± 0.040	27 ± 2			
A13C8	0.703 ± 0.048	27 ± 3	0.782 ± 0.020	23 ± 1	4
C14C5	0.769 ± 0.054	24 ± 3	0.741 ± 0.015	25 ± 1	−2
C14C6	0.841 ± 0.064	19 ± 4	0.896 ± 0.023	15 ± 2	4
MAf adduct motional model					
T4C6	0.744 ± 0.132	25 ± 8			
HMT-C3	0.704 ± 0.040	27 ± 2			
HMT-C5	0.823 ± 0.056	20 ± 4			

and A5(13)C2 spins relative to the A5(13)C1′ are also observed (Table 1). The S^2 for the C5 and C6 spins in each of the cytosine bases in the UM have different values. The largest difference is for the UM C6(14)C6 and C6(14)C5 atoms. This is interesting because the values bracket the relatively low S^2 for the UM C6(14)C1′. In both the UM and the MAf the C6(14)C5 atom is less ordered than the adjacent C6(14)C6 atom. While these cytosine base atoms are covalently connected as part of a rigid aromatic system, the C−H bond vectors point in different directions. Pivoting of the base around the glycosidic bond should subject the C6−H6 and the C5−H5 bond vector to the same amplitude motions on an identical time scale. In a simple motional model, the direct attachment of the C1′ to the base means that translational motions of the base equally affect the order of the adjacent C1′ spin. In this model, only rotations about the glycosidic bond, χ, could make S^2(C1′) different from S^2(C8,2,6,5). These results suggest that a more complicated motional model must be considered to account for the observed discrepancy. Unfortunately, the current data are insufficient to develop a more complex model that is valid in these systems.

Motional Model for the HMT-T Adduct. The T4 base is connected to the furan ring of the HMT in the MAf through a cyclobutane ring forming a relatively rigid 5-ring system (**2**) as shown in Figure 1. There are three methine carbons in this adducted residue, HMT-C3 and HMT-C5 and T4C6, which is one of the carbons in the cyclobutane ring. Both of the HMT carbons are in the rigid aromatic pyrone portion of the MAf, but their C−H bond vectors point in different directions with respect to the helix axis of the molecule. Interestingly, all three of these carbons show different values for S^2, with the T4C6 and HMT-C3 both lower than the HMT-C5 (Table 3, Figure 4B). We can use these model-free results to develop a simple and specific motional model to explain the differences in the S^2 values for this rigid moiety. A rocking motion about the T4 glycosidic bond will cause both the T4C6−H6 and the HMT-C3−H3 bond vectors to move through space while the HMT-C5−H5 bond vector remains essentially motionless (Figure 6). This rocking motion would necessarily displace the attached C1′ atom. The MAf T4C1′ is a very disordered atom, with an $S^2 = 0.645 \pm 0.059$ and a substantial chemical exchange term of $5.02 \pm 2.53\ s^{-1}$, supporting the model. The rocking motion also appears to be propagated to the residues on the *unadducted* strand. Four atoms, T12C6, HMT-C3, A13C8, and C14C5, are in direct contact with each other and are approximately stacked up in a line (see Figure 7 with the lineup of red atoms compared to the UM). The order parameter for the MAf T12C6 is 0.206 unit lower than the corresponding atom in the UM and the MAf A13C8 is 0.079 unit lower than in the UM. The order parameters for the flanking C14C5 and C14C6 are essentially the same in both molecules. It appears that the MAf formation reduces the order of the adjacent atoms and "smoothes" out the values when compared to the parent UM. The formation of the MAf changes the twist at the TpA step to 27° and the A5-C6 step to 30° from 36° found in canonical B-form DNA. The HMT C3 is in van der Waals contact with and serves as a bridge between the T12C6 and A13C8 atoms. In the UM, the twist at the TpA step is more standard, and the corresponding atoms are displaced relative to one another and are not in van der Waals contact. The relative twist at the MAf A13-C14 and the UM A5-C6 steps are very similar, and there is a correspondingly smaller difference in the order parameters for the atoms at this step for these two molecules.

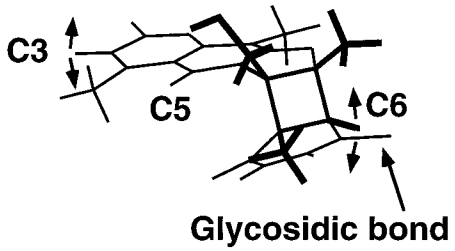

FIGURE 6: MAf showing the possible mechanism for motion. Rotation about the glycosidic bond (N1−C1′) causes a correlated displacement of the HMT-C3 and T4C6 atoms while the HMT-C5−H5 bond vector remains essentially motionless. The direction of the rocking motion is indicated for the HMT-C3−H6 and T4C6−H6 bond vectors by the double-headed arrows. The glycosidic bond is indicated by the single-headed arrow.

The order parameter (S^2) correlates with the semiangle θ of the "wobbling in a cone" model, according to $S^2 = [\cos\theta\,(1 + \cos\theta)/2]^2$ (*67*). Table 3 shows the order parameters and semiangle of the cone using this simple diffusion model for the four lined-up spins in the MAf and for the three spins of the HMT-T4 adduct (Figure 7).

While the atoms in the MAf T4 have significantly altered dynamics with respect to those in the UM T4, there are almost no changes between the UM and the MAf in S^2 for the flanking residues G3 and A5 (Tables 1 and 2). Structurally, the residues flanking the HMT adduct on the damaged strand are G3 and A5 because the pyrimidine base T4 is an integral part of the HMT adduct. The HMT-adducted T4 forms an imperfect stack with the neighboring base G3 because cyclobutane ring formation changes the hybridization of the T4C5 and T4C6 from sp^2 to sp^3 that forces the methyl group (5-Me) and 6-H of the adducted thymidine away from the HMT. The adjacent base of G3 maintains stacking interactions by making contact with the "folded thymidine"

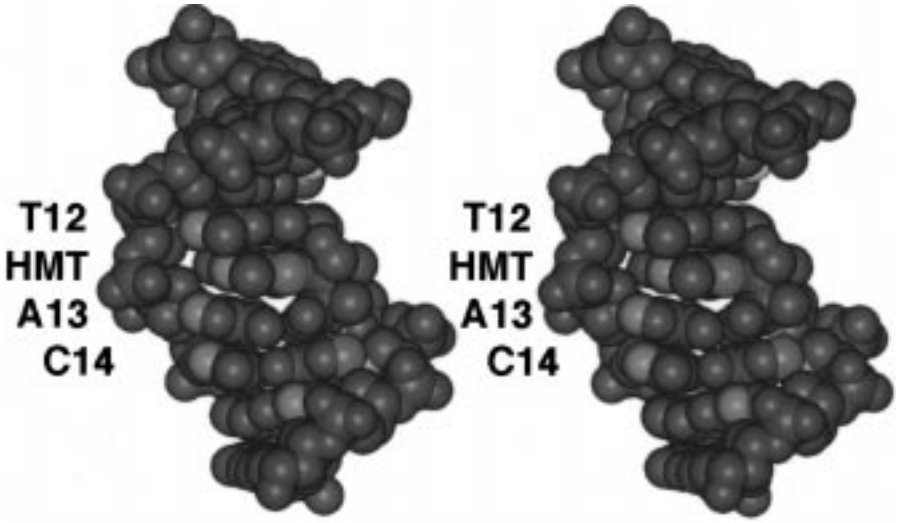

FIGURE 7: Stereoview of the space-filling model of the MAf viewed into the major groove showing the unadducted strand and pyrone side of the HMT color-coded by the value of the generalized order parameter where the protons have been omitted for clarity. Note the alignment of the aromatic carbon atoms colored red. The HMT adduct is indicated. The color scheme is as follows: blue, S^2 not determined; cyan, $S^2 \geq 0.85$; green, $0.85 \geq S^2 \geq 0.75$; red, $0.75 \geq S^2 \geq 0.65$; yellow, $S^2 \leq 0.65$.

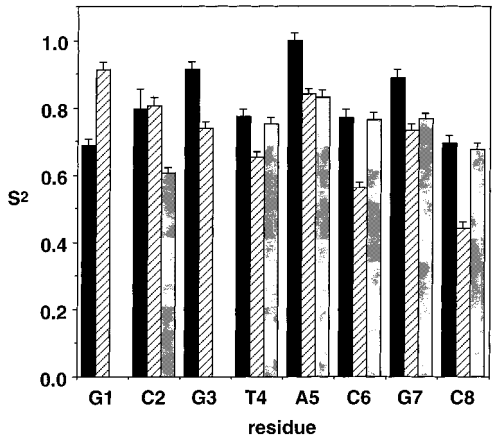

FIGURE 8: Model-free derived order parameters for the deoxyribose methine carbons in the UM. For each residue the S^2 for C1′ is shown in solid black, the S^2 for C3′ is striped, and the S^2 for C4′ is in gray. Data are from Table 1.

base of T4 at the 5-methyl, O2, and N3H (*40*). The major change in dynamics at this interface is the quenching of microsecond to millisecond dynamics inferred from the ability to fit the relaxation data for the MAf spins without the chemical exchange term required for the corresponding UM spins. The observations of highly localized changes in dynamic behavior for the MAf adducted strand are in contrast to the MAf unadducted strand where it appears that adduct formation drives a general lowering of order parameters for residues T12 and A13 flanking the adduct.

DISCUSSION

The solution structures of both the MAf and the UM (data not shown) have been determined by NOE-driven means and give a high-resolution time-averaged picture of the organization of the TpA step where the HMT damage has its greatest impact (*40*, *41*).

Analysis of ^{1}H COSY spectra of the MAf provided evidence for altered dynamics or additional conformations for the T4, A5, T12, and A13 deoxyriboses at the site of adduction relative to those of the UM (*54*). For the MAf T4C1′, T12C1′, and the A13C1′ atoms there is a significant decrease in their order parameters relative to the corresponding spins in the UM (Table 3). These results support a previous analysis that suggested unusual dynamics in the backbone of the psoralen-modified DNA when compared with unmodified DNA. HMT photoaddition to the UM appears to destabilize the preference for the usual C2′-*endo* sugar conformation of the four nucleotides, T4, A5, T12, and A13, permitting them to adopt a larger range of rapidly interconverting conformers.

In the UM there is a rough correlation of the C1′ order parameters with base type. Purine residues have higher S^2 values than the pyrimidine residues. This same rough trend is followed by the C3′ order parameters, but not for the C4′ order parameters. Previous ^{1}H NMR studies of other alternating purine−pyrimidine sequences have noted alternating sugar puckers and/or the existence of multiple interconverting sugar puckers and alternating backbone conformational differences (*76*−*79*).

Unlike Borer et al. (*5*), we do not find that the base order parameters for the terminal nucleotides are lower than for the central residues. The order parameters are quite high and relatively uniform over the length of the molecule, suggesting that "end effects" are not important for high-frequency internal motions. However, the 3′-terminal C8 deoxyribose spins are on average lower than the rest of the molecule (Table 1, Figure 4A). In the earlier study, the data were collected by direct detection of ^{13}C by 1D NMR for NOE and R_1. The present study involved the measurement of a third parameter—R_2—which allows for a more complete description of the system. The values found for the effective internal correlation time, τ_f, in the UM and MAf, which range up to 91 ps, agree with the values estimated by Borer et al. (*5*) for sugar and base motions (30−300 ps) and with those of Gaudin et al. (*15*) for an internal diffusion coefficient of 30×10^7 s^{-1} for a restricted rotation model about the glycosidic bond with $\Delta\chi = 28°$. It is possible that the DNA forms transient end-to-end stacked aggregates at the relatively high DNA concentrations used in these studies, which may alter the motional freedom of the terminal residues. How-

ever, the self-consistent theoretical, homo- and heteronuclear-derived τ_m values argue against this being a major effect. Differences in results may also reflect sequence-dependent effects.

The pulse sequence used to measure R_2 in this study does not account for the cross-correlation (interference) between the CSA and dipolar relaxation mechanisms. The cross-correlation for aliphatic carbons can be neglected because the CSA contribution to relaxation is small compared to the dipolar contribution. Because the CSA for the aromatic carbons is much larger, there is a correspondingly larger interference between the CSA and dipolar relaxation mechanisms. The magnitude of this interference on R_2 can be calculated (*59*). For the aromatic carbons, the calculated effect would increase the measured R_2 by approximately 24% for a CSA of 185 ppm and 4% for a CSA of 41 ppm. The conclusions of the study are not altered if these adjusted numbers are used in the calculations of S^2. However, the calculated order parameters for the aromatic spins are somewhat higher.

The current analysis is a limited description of the dynamic modes that characterize the complex conformational equilibria of these two DNA molecules in solution. The primary limitation of this approach is that the complex equilibria are oversimplified by the model-free approach and because the problem is in general underdetermined. However, the results obtained in this study suggest that model-free analysis coupled with the physical constraints of the system being studied can yield tentative physical models. For each sugar residue under ideal conditions, order parameters for the three ring methine carbons can be determined, and the base C8, C6, C2, and C5 carbon order parameters can be correlated with the sugar residue through the motion of the base relative to the sugar about the glycosidic bond. The constraints imposed on the system by these coupled order parameters should allow us to constrain the potential motions available to the polymer by more than simply attempting to rationalize the significance of the order parameters for the individual C−H vectors alone in isolation. An example of this is shown in Figure 7, where a possible correlation of the motions of stacked aromatic systems in the MAf is evident. The order parameters in the MAf for the T12C6, HMT-C3, A13C8, and C14−C6 are all the same magnitude. The order parameters for these spins have much more divergent values in the UM. In fact, there is a marked decrease in the order parameters at the site of damage. More complete motional models can be tested by mapping the spectral density function of the spins. However, this approach requires further investigation with ^{13}C isotopically enriched molecules.

Biological Consequences. Structures of damaged DNA substrates complexed with any components of either prokaryotic or eukaryotic components of the NER system have not been determined, nor are any structures of the protein components of the NER system known. Because the MAf is recognized by both the human repair system and the prokaryotic (A)BC excinuclease, it serves as an excellent model to study the structural and dynamic motifs that cellular repair enzyme systems may recognize (*17*, *40*, *41*, *43*, *44*). Comparisons of the structural and dynamic differences between the UM and the MAf allow for examination of features that may be recognized by the enzyme system. Understanding how the NER excinuclease recognizes psoralen damage to DNA will assist in the elucidation of the general mechanism of lesion recognition.

There appears to be an alteration of the base stacking due to the monoaddition as evidenced by the apparent correlated changes in the order parameters in Figure 7 (where the carbon atoms colored red line up). The recognition of the lesion by the enzyme system may be sensitive to these changes in conformation indicated by the greater amplitude of picosecond to nanosecond dynamics in and around the damage site. Additionally, there is a large change in the chemical exchange components in and around the site of damage. The substantial changes in the order parameters and chemical exchange components for both T4 and T12 indicate the presence of additional non-B-like DNA conformations that may be accessible to the MAf that may serve as potential recognition motifs for the NER system.

A singular aspect of NER is the ability of the enzyme system to position itself to the site of damage and direct only the excision of the damage. The observation that the adducted T4 is highly destabilized in the MAf while the order parameters for the two flanking residues are hardly affected suggests a mechanism which may allow the NER system to localize itself to the damage. The MAf T4C1′ has a low S^2 and a significant chemical exchange component. By analogy with the relationship of the C3′ and C4′ spins to the C1′ spin in residues in the UM, we expect that the MAf T4C3′ and C4′ spins will also have a very low S^2. This implies multiple rapidly interconverting conformations in the backbone of the DNA at the site of damage, some of which may not be significantly populated or energetically accessible in the native DNA. This proposed mechanism does not preclude the possibility that the enzyme system is also recognizing the "softness" of the undamaged strand as evidenced by the general decrease measured in S^2 for the undamaged strand.

These conclusions are supported by previous homonuclear studies that have compared the conformations of the UM sugars with those of MAf and XL. In those studies it was found that the HMT damage destabilizes the preference for C2′-*endo* sugar conformation of the four nucleotides T4, A5, T12, and A13. The MAf or XL permits them to adopt a larger range of rapidly interconverting conformers with a significantly altered population distribution with respect to unmodified DNA (*40*, *54*). These changes in the equilibrium distribution of the deoxyribose conformations and the implied coupled "crankshaft motions" of the phosphate backbone detected for the MAf and XL may be recognized as the signal that positions the DNA repair system at the location of the DNA damage.

The DNA repair system in this model recognizes changes in the equilibrium behavior of the DNA surrounding the adduct, not specific structural features induced by the damage (*20*, *52*). Other DNA oligomers covalently modified with drugs that are recognized by cellular repair systems and have radically different structures from the MAf and the XL show evidence of altered helix dynamics by NMR (*80*).

The analysis presented here supports the hypothesis that the backbone of undamaged DNA has a certain rigidity that is ignored by the NER system and that introduction of a region of greater conformational freedom into the DNA backbone at the adduct is recognized as damage by the NER complex. Determination of the precise backbone dynamic

modes that are changed by lesion formation will require further experiments that provide information on the precise form of the additional conformational freedom available to these molecules.

ACKNOWLEDGMENT

We thank Professor Jöel Mispelter (INSERM, Orsay) for providing the pulse sequences that we modified to accomplish this work, Professor Arthur G. Palmer, III (Columbia University, New York) for providing ModelFree and many helpful discussions, Dr. Sue Wollowitz (Cerus Corp., Concord, CA) for the generous gift of HMT, and Professor David Rodgers (University of Kentucky) and Professor Trevor Creamer (University Kentucky) for careful reading of the manuscript.

REFERENCES

1. Hogan, M. E., and Jardetzky, O. (1979) *Proc. Natl. Acad. Sci. U.S.A. 76*, 6341−6345.
2. Hogan, M. E., and Jardetzky, O. (1980) *Biochemistry 19*, 2079−2085.
3. Hogan, M. E., and Jardetzky, O. (1980) *Biochemistry 19*, 3460−3468.
4. Keepers, J. W., and James, T. L. (1982) *J. Am. Chem. Soc. 104*, 929−939.
5. Borer, P. N., LaPlante, S. R., Kumar, A., Zanatta, N., Martin, A., Hakkinen, A., and Levy, G. C. (1994) *Biochemistry 33*, 2441−2450.
6. Kochoyan, M., Leroy, J. L., and Gueron, M. (1987) *J. Mol. Biol. 196*, 599−609.
7. Gueron, M., Kochoyan, M., and Leroy, J. L. (1987) *Nature 328*, 89−92.
8. Briki, F., Ramstein, J., Lavery, R., and Genest, D. (1991) *J. Am. Chem. Soc. 113*, 2490−2493.
9. Brooks, C. L., III, Karplus, M., and Pettitt, B. M. (1988) *Proteins: A Theoretical Perspective of Dynamics, Structure, and Thermodynamics*, J. Wiley & Sons, New York.
10. Bax, A., Sparks, S. W., and Torchia, D. A. (1989) *Methods Enzymol. 176*, 134−150.
11. Nirmala, N. R., and Wagner, G. (1988) *J. Am. Chem. Soc. 110*, 7557−7558.
12. Palmer, A. G., III, Rance, M., and Wright, P. E. (1991) *J. Am. Chem. Soc. 113*, 4371−4380.
13. Alattia, T., Padilla, A., and Cavè, A. (1996) *Eur. J. Biochem. 237*, 561−574.
14. Mispelter, J., Lefevre, C., Adjadj, E., Quiniou, E., and Favaudon, V. (1995) *J. Biomol. NMR 5*, 233−244.
15. Gaudin, F., Paquet, F., Chanteloup, L., Beau, J. M., Nguyen, T. T., and Lancelot, G. (1995) *J. Biomol. NMR 5*, 9−58.
16. Sancar, A., (1994) *Science 266*, 1954−1956.
17. Sancar, A., and Sancar, G. B. (1988) *Annu. Rev. Biochem. 57*, 29−67.
18. Van Houten, B. (1990) *Microbiol. Rev. 54*, 18−51.
19. Grossman, L., and Thiagalingam, S. (1993) *J. Biol. Chem. 268*, 16871−16874.
20. Lin, J. J., and Sancar, A. (1989) *Biochemistry 28*, 7979−7984.
21. Huang, J. C., Hsu, D. S., Kazantsev, A., and Sancar, A. (1994) *Proc. Natl. Acad. Sci. U.S.A. 91*, 12213−12217.
22. Cassier, C., Chanet, R., and Moustacchi, E. (1984) *Photochem. Photobiol. 39*, 799−803.
23. Fujita, H. (1984) *Photochem. Photobiol. 39*, 835−839.
24. Misra, R. R., and Vos, J. M. (1993) *Mol. Cell Biol. 13*, 1002−1012.
25. Sage, E., Drobetsky, E. A., and Moustacchi, E. (1993) *EMBO J. 12*, 397−402.
26. Yang, S. C., Lin, J. G., Chiou, C. C., Chen, L. Y., and Yang, J. L. (1994) *Carcinogenesis 15*, 201−207.
27. Corash, L., Lin, L., and Wiesehahn, G. (1992) *Blood Cells 18*, 57−74.
28. Morel, P., Lin, L., Wiesehahn, G., and Corash, L. (1992) *Blood Cells 18*, 27−42.
29. Lin, L., Londe, H., Hanson, C. V., Wiesehahn, G., Issacs, S., Cimino, G., and Corash, L. (1993) *Blood 82*, 292−297.
30. Lin, L., Cook, D. N., Wiesehahn, G., Alfonso, R., Behrman, B., Cimino, G. D., Corten, L., Damonte, P. B., Dikeman, R., Dupis, K., Fang, Y. M., Hanson, C. V., Hearst, J. E., Lin, C. Y., Londe, H., Metchette, K., Nerio, A. T., Pu, J. T., Reames, M., Rheinschmidt, M., Tessman, J., Issacs, S., Wollowitz, S., and Corash, L. (1997) *Transfusion 37*, 423−435.
31. Straub, K., Kanne, D., Hearst, J. E., and Rapoport, H. (1981) *J. Am. Chem. Soc. 103*, 2347−2355.
32. Kanne, D., Straub, K., Hearst, J. E., and Rapoport, H. (1982) *J. Am. Chem. Soc. 104*, 6754−6764.
33. Kanne, D., Straub, K., Rapoport, H. and Hearst, J. E. (1982) *Biochemistry 21*, 861−871.
34. Shi, Y., Lipson, S., Chi, D. Y., Spielmann, H. P., Monforte, J., and Hearst, J. E. (1990) Applications of Psoralens as Probes of Nucleic Acid Structure and Function, *Bioorganic Photochemistry: Photochemistry and the Nucleic Acids*, 1st ed., pp 341−378, J. Wiley & Sons, New York.
35. del Olmo, M. L., Sogo, J. M., Franco, L., and Perez-Ortin, J. E. (1993) *Yeast 9*, 1229−1240.
36. Sastry, S. S., Spielmann, H. P., Hoang, Q. S., Phillips, A. M., Sancar, A. and Hearst, J. E. (1993) *Biochemistry 32*, 5526−5538.
37. Huang, J. C., and Sancar, A. (1994) *J. Biol. Chem. 269*, 19034−19040.
38. Islas, A. L., Baker, F. J., and Hanawalt, P. C. (1994) *Biochemistry 33*, 10794−9.
39. Ramaswamy, M., and Yeung, A. T. (1994) *J. Biol. Chem. 269*, 485−492.
40. Spielmann, H. P., Dwyer, T. J., Sastry, S. S., Hearst, J. E., and Wemmer, D. E. (1995) *Proc. Natl. Acad. Sci. U.S.A. 92*, 2345−2349.
41. Spielmann, H. P., Dwyer, T. J., Hearst, J. E., and Wemmer, D. E. (1995) *Biochemistry 34*, 12937−12953.
42. Spielmann, H. P., Chi, D. Y., Hunt, N., Klein, M. P., and Hearst, J. E. (1995) *Biochemistry 34*, 14801−14814.
43. Cheng, S., Van Houten, B., Gamper, H., Sancar, A., and Hearst, J. E. (1988) *J. Biol. Chem. 263*, 15110−15117.
44. Cheng, S., Sancar, A., and Hearst, J. E. (1991) *Nucleic Acids Res. 19*, 657−663.
45. Van Houten, B., Gamper, H., Holbrook, S., Sancar, A., and Hearst, J. E. (1986) *Proc. Natl. Acad. Sci. U.S.A. 83*, 8077−8081.
46. Smith, C. A. (1988). Repair of DNA Containing Furocoumarin Adducts, *Psoralen DNA Photobiology*, pp 87−116, CRC Press, Inc., Boca Raton, FL.
47. Van Houten, B., Gamper, H., Sancar, A. and Hearst, J. E. (1988) *J. Biol. Chem. 263*, 16553−16560.
48. Cheng, S., Van Houten, B., Gamper, H., Sancar, A., and Hearst, J. E. (1988) Use of Triple-Stranded DNA Complexes to Study Cross-link Repair, *Mechanisms and Consequences of DNA Damage Processing*, pp 105−113, Alan R. Liss, New York.
49. Sladek, F. M., Munn, M. M., Rupp, W. D., and Howard-Flanders, P. (1989) *J. Biol. Chem. 264*, 6755−6765.
50. Smith, K. C., Wang, T.-C. V., and Sharma, R. C. (1989) *BioEssays 10*, 12−16.
51. Van Houten, B., and Snowden, A. (1993) *Bioessays 15*, 51−59.
52. Pu, W. T., Kahn, R., Munn, M. M., and Rupp, W. D. (1989) *J. Biol. Chem. 264*, 20697−704.
53. Williams, L. D., and Gao, Q. (1992) *Biochemistry 31*, 4315−4324.
54. Emsley, L., Dwyer, T. J., Spielmann, H. P., and Wemmer, D. E. (1993) *J. Am. Chem. Soc. 115*, 7765−7771.
55. Spielmann, H. P., Sastry, S. S., and Hearst, J. E. (1992) *Proc. Natl. Acad. Sci. U.S.A. 89*, 4514−4518.
56. Delsuc, M. A., and Lallemand, J. Y. (1986) *J. Magn. Reson. 69*, 504−507.
57. States, D. J., Haberkorn, R. A., and Ruben, D. J. (1982) *J. Magn. Reson. 48*, 286−292.

58. Schmieder, P., Ippel, J. H., van den Elst, H., van der Marel, G. A., Altona, C., and Kessler, H. (1992) *Nucleic Acids Res. 20*, 4747−4751.
59. Palmer, A. G., III, Skelton, N. J., Chazin, W. J., Wright, P. E., and Rance, M. (1992) *Mol. Phys. 75*, 699−711.
60. Palmer, A. G., III, Hochstrasser, R. A., Millar, D. P., Rance, M., and Wright, P. E. (1993) *J. Am. Chem. Soc. 115*, 6333−6345.
61. Mandel, A. M., Akke, M., and Palmer, A. G., III (1995) *J. Mol. Biol. 246*, 144−163.
62. Bevington, P. R. (1969) *Data Reduction and Error Analysis for the Physical Sciences*, McGraw-Hill, New York.
63. Abragam, A. (1968) *The Principles of Nuclear Magnetism*, Clarendon Press, Oxford.
64. Kay, L. E., Torchia, D. A., and Bax, A. (1989) *Biochemistry 28*, 8972−8979.
65. Williamson, J. R., and Boxer, S. G. (1988) *Nucleic Acids Res. 16*, 1529−1540.
66. Lipari, G., and Szabo, A. J. (1982) *J. Am. Chem. Soc. 104*, 4546−4559.
67. Lipari, G., and Szabo, A. J. (1982) *J. Am. Chem. Soc. 104*, 4559−4570.
68. Clore, G. M., Szabo, A., Bax, A., Kay, L. E., Driscoll, P. C., and Gronenborn, A. M. (1990) *J. Am. Chem. Soc. 112*, 4989−4991.
69. Bloom, M., Reeves, L. W., and Wells, E. J. (1965) *J. Chem. Phys. 42*, 1615−1624.
70. Liu, H., Spielmann, H. P., Ulyanov, N. B., Wemmer, D. E., and James, T. L. (1995) *J. Biomol. NMR 6*, 390−402.
71. Eimer, W., Williamson, J. R., Boxer, S. G., and Pecora, R. (1990) *Biochemistry 29*, 799−811.
72. SantaLucia, J., Jr., Allawi, H. T., and Seneviratne, P. A. (1996) *Biochemistry 35*, 3555−3562.
73. Kennedy, M. A., Nuutero, S. T., Davis, J. T., Drobny, G. P., and Reid, B. R. (1993) *Biochemistry 32*, 8022−8035.
74. Lingbeck, J., Kubinec, M. G., Miller, J., Reid, B. R., Drobny, G. P., and Kennedy, M. A. (1996) *Biochemistry 35*, 719−734.
75. McAteer, K., Ellis, P. D., and Kennedy, M. A. (1995) *Nucleic Acids Res. 23*, 3962−3966.
76. Schmitz, U., Zon, G., and James, T. L. (1990) *Biochemistry 29*, 2357−2368.
77. Schmitz, U., Pearlman, D. A., and James, T. L. (1991) *J. Mol. Biol. 221*, 271−292.
78. Gochin, M., Zon, G., and James, T. L. (1990) *Biochemistry 29*, 11161−11171.
79. Gochin, M., and James, T. L. (1990) *Biochemistry 29*, 11172−11180.
80. O'Handley, S. F., Sanford, D. G., Xu, R., Lester, C. C., Hingerty, B. E., Broyde, S., and Krugh, T. R. (1993) *Biochemistry 32*, 2481−2497.

BI972536B